Proceedings Paper:

This is an author produced version of a paper presented at ICMF 2019.

Simulation of Fully Resolved Particle-Particle Interactions in Turbulence with Behavioural Modification

L.F. Mortimer, M. Fairweather, D.O. Njobuenwu

School of Chemical and Process Engineering.

University of Leeds, Leeds, LS2 9JT, United Kingdom

l.f.mortimer@leeds.ac.uk, m.fairweather@leeds.ac.uk, d.o.njobuenwu@leeds.ac.uk

Abstract

Fully resolved particle-particle interaction events in turbulence are studied using high fidelity simulation. The continuous phase uses a spectral element-based direct numerical simulation and the discrete phase is modelled using the immersed boundary method. The ghost-cell technique is used to achieve particle-fluid coupling and the method is validated against empirically determined drag coefficients with strong agreement for high resolution particle meshes. The interactions take place in an isotropic box of turbulence at Reynolds number (based on the Taylor microscale), $Re_\lambda = 51$. This value is selected to closely resemble those typical of the buffer layer in a turbulent channel flow at shear Reynolds number, $Re_\tau = 180$. Particulate phase properties are chosen to represent $100\ \mu m$ diameter calcite particles in water, but the chemical and dynamic properties of both phases are varied to determine the extent of behavioural modification through alteration of these parameters. Results indicate that the restitution coefficient has the greatest effect on collision dynamics, with an increase leading to fewer particle agglomerations. Reducing the Hamaker constant has a lesser effect on the resulting interaction but does lower the mean speed of the particles undergoing collision. The electric double layer potential has very little effect on any of the agglomeration dynamics, since its strength and effective range is much lower than that of the van der Waals component. Suggestions are offered for behavioural modification techniques based on the present results.

Introduction

Particle-laden turbulent flows are prevalent in many natural and industrial environments. The ability to predict complex multiphase flows such as tidal currents (Wang et al. 2010), lung airways (Walters & Luke, 2010) and liquid-fueled combustion (Gosman & Ioannides 1983) rely heavily on an understanding of the fundamental particle-scale dynamics and interactions. The present work is of relevance to the nuclear industry, where current reactor cooling and waste processing systems could be improved through behavioural modification techniques. These aim to improve the flow conditions by controlling the mechanical and chemical properties of the system through injected additives such as polymers (den Toonder et al. 1997), which can result in reduced or enhanced aggregation depending on the desired outcome. Furthermore, understanding behind agglomeration mechanisms involved in the build-up of CRUD (Chalk-River unidentified deposits) on reactor fuel-pins (Short et al. 2013) can be developed by studying such models, providing a means to improve performance and safety.

Precisely modelling particle interactions at micron-scales has long been challenging, but recent advances in computational power now allow for realistic simulations at increased levels of accuracy. This allows for the generation of understanding of multiphase flows at a more fundamental level, hence this has been of great interest in the recent literature. Whilst the combination of direct numerical simulation (DNS) of the continuous phase with Lagrangian particle tracking (LPT) of the discrete phase is frequently used to simulate such systems, in this approach, despite all relevant length-scales being resolved in the Eulerian phase, the point-like constraint on the particulate phase means that information surrounding the small-scale fluid-structure interactions is lost. To overcome this, higher fidelity simulations using models based on empirical observations are used to provide quantities as the drag and lift force coefficients which estimate the local fluid flow field influence on the particle. This approach is more suited to studying huge ensembles of particles $(N_P \sim 10^6)$, within which mean quantities can be studied to understand macroscopic behaviour. For a more fundamental approach, and to fully determine the dynamics of small-scale motion and interaction (which underpin the large scales), we must fully resolve the flow field surrounding the particles. The approaches which allow this to be achieved are referred to commonly as interface tracking techniques. Various such computational methods and algorithms have been developed over the last few decades (Mark & van Wachem 2008, Tseng & Ferziger 2003, Peskin 2002, Hu, 1996), each of which offers its own trade-off between accuracy and computational complexity.

This work uses a ghost-cell based immersed boundary method (IBM) coupled to a spectral element method (SEM) based DNS solver to fully resolve the flow around dynamic particle meshes. The aim is to study the effect that varying certain chemical and mechanical properties has on the resulting particle interaction dynamics. Particle collision events are

modelled and initialized based on those most frequently occurring in the buffer layer of a $Re_\tau = 180$ turbulent channel flow. A DLVO theory-based potential is used to determine the particle-particle interaction forces at short ranges. By analysing the resulting trajectories and dynamic properties of these two-particle systems, understanding can be developed on how (and under what conditions) particle collisions or agglomerations occur, at levels of detail which greatly surpass those of LPT-based studies. Suggestions are also offered for realistic behavioural modification techniques that might be applied in practice.

Numerical Methods

A. Linearly forced homogeneous isotropic turbulence

The continuous phase dynamics are governed by the incompressible Navier-Stokes equations, solved using the spectral-element method-based DNS solver, Nek5000 (Fischer et al., 2008). The flow equations are:

$$\boldsymbol{\nabla} \cdot \boldsymbol{u}_F = 0, \qquad (1)$$

$$\frac{\partial \boldsymbol{u}_F}{\partial t} + \boldsymbol{u}_F \cdot \boldsymbol{\nabla} \boldsymbol{u}_F = -\frac{\boldsymbol{\nabla} p}{\rho_F} + \frac{1}{\rho_F} \boldsymbol{\nabla} \cdot \boldsymbol{\tau} + \boldsymbol{f}_{LF}. \qquad (2)$$

Here, $\boldsymbol{u}_F(\boldsymbol{x}, t)$ is the fluid velocity vector at position vector $\boldsymbol{x}$, t is the time, p is the pressure, ρ_F is the continuous phase density, and $\boldsymbol{\tau}$ is the deviatoric stress tensor for a Newtonian fluid. The acceleration, $\boldsymbol{f}_{LF}$, is a linear forcing source term determined such that the mean and root-mean-square of the turbulent fluctuations remain stationary. The geometry for all simulations is a cube of length 2π with periodic boundary conditions at $\pm\pi$, consisting of 48^3 spectral elements of equal size and distribution. A schematic of the setup is provided in Fig. 1. The solution polynomial order for the SEM is $N = 7$. All simulations were performed on 120 compute nodes using the Advanced Research Computing HPC service at the University of Leeds.

The linear forcing method (Rosales & Meneveau 2005, Lundgren 2003) was used to drive the system to isotropic homogenous turbulence at Reynolds number (based on the Taylor microscale, λ), $Re_\lambda = 51$, where $Re_\lambda = \langle u_{rms}' \rangle \lambda / \nu_F$. Here, $\langle u_{rms}' \rangle$ is the averaged root mean square velocity fluctuation and ν_F is the kinematic viscosity of the fluid. In a turbulent channel flow, this Reynolds number is typical of that present within the buffer layer region. Previous work has demonstrated that collisions are more frequent within this region, particularly for large solid-fluid density ratios or inertial particles (Mortimer et al. 2018).

The linear force per unit mass term is given by $\boldsymbol{f}_{LF} = A\boldsymbol{u}_F$, where A is a specified parameter relating to an eddy turnover time scale. Tuning of this parameter allows one to obtain a desired turbulence level. The fluid phase parameters used are presented in Table 1.
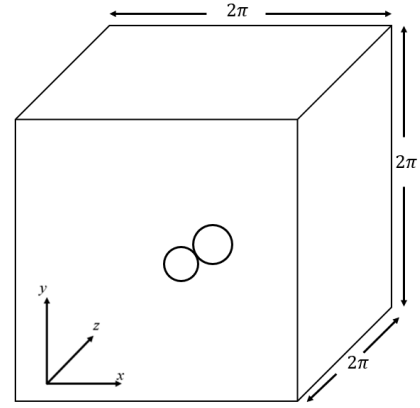

Figure 1: Schematic of particle-particle interaction event occurring in homogeneous isotropic box of periodic turbulence.

Table 1: DNS parameters for periodic cube of linearly forced homogeneous isotropic turbulence.

Re_λ	51
N_E	48^3
A	0.2
Δt	1×10^{-3}
ρ_F	1
ν_F	4.491×10^{-3}

B. Ghost-cell based immersed boundary method

A computational icosphere mesh is used to represent each particle, which is stored in the face-vertex representation and consists of 320 faces. An example of this is presented in Fig. 2. Each face has an associated centroid position and velocity (where the velocity is derived from the global particle angular velocity).
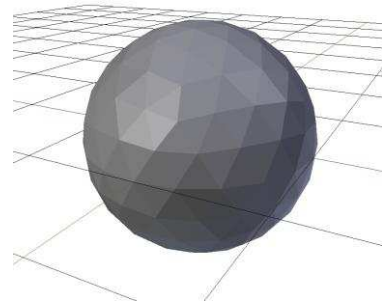
Figure 2: Computational icosphere mesh made up of 320 faces representing immersed boundary for spherical particle.

The immersed boundary (IB) condition is a Dirichlet condition such that $\boldsymbol{u}_F = \boldsymbol{u}_P + \boldsymbol{\omega}_P \times \boldsymbol{r}_f$ on each particle face, f. Here, $\boldsymbol{u}_{P,f}$ is the particle linear velocity, $\boldsymbol{\omega}_P$ is the particle angular velocity and $\boldsymbol{r}_F$ is the position vector from the centre of the particle to the centroid of face F (Peskin, 2002).

To ensure the IB condition is met, a second-order accurate ghost cell method is used. Every timestep, each cell in the domain (formed by the bisectors between two neighbouring Gauss-Lobatto-Legendre (GLL) points, which are the fluid interpolation points associated with the SEM) is identified as external fluid, an internal ghost-cell or internal fictitious fluid. A ghost cell is defined such that the IB intersects the cell and contains the cell midpoint. Internal and external fluid cells are those either inside or outside the IB, respectively. This is illustrated in Fig. 3. The velocities at the ghost-cells are maintained each timestep such that, through trilinear interpolation across the three closest neighbouring cells, the fluid velocity on the boundary is exactly the local face velocity.
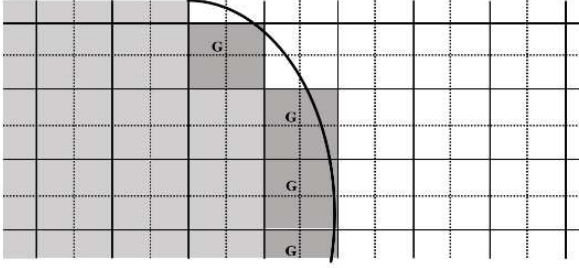

Figure 3: Computational domain schematic containing an immersed boundary. Dotted lines meet at GLL points. White cells represent external fluid domain, whilst light grey cells are interior points. Remaining grey cells identified by 'G' represent the ghost cell domain.

To advect and rotate the particle, pressure and viscous surface forces and torques are calculated using the local fluid pressure and viscous stress tensor. The equation for the hydrodynamic force exerted on face j, F_j, is:

$$F_j = \sum_{f=1}^{N_f} \left(\underbrace{-P^f \delta_{ij}}_{Pressure} + \underbrace{\tau_{ij}^f}_{Viscous} \right) n_j^f \, dS^f. \qquad (3)$$

Here, F is the total translational force on the particle, f refers to the current face in the summation, with N_f being the total number of faces in the particle mesh, P is the pressure interpolated at the face centroid, τ is the viscous stress tensor, n is a unit vector normal to the face, and dS is the surface area of the face. A similar equation is used to calculate the viscous contributions to torque in the off-normal directions, used to update the angular velocity of the particle.

Particle orientation is tracked using the quaternion formulation. Each timestep the quaternion vector $Q = (q_0, q_1, q_2, q_3)$, and the angular velocity vector (in the particle co-moving reference frame) $\omega_P = (\omega_{x'}, \omega_{y'}, \omega_{z'})$, are also tracked. The time-varying quaternion vector differential equation is:

$$\frac{d\boldsymbol{Q}}{dt} = \begin{pmatrix} \frac{dq_0}{dt} \\ \frac{dq_1}{dt} \\ \frac{dq_2}{dt} \\ \frac{dq_3}{dt} \end{pmatrix} = \begin{pmatrix} q_0 & -q_1 & -q_2 & -q_3 \\ q_1 & q_0 & -q_3 & q_2 \\ q_2 & q_3 & q_0 & -q_1 \\ q_3 & -q_2 & q_1 & q_0 \end{pmatrix} \begin{pmatrix} 0 \\ \omega_{x'} \\ \omega_{y'} \\ \omega_{z'} \end{pmatrix}, \qquad (4)$$

and the corresponding Eulerian torque equation is given by:

$$I \frac{d\boldsymbol{\omega}}{dt} = \boldsymbol{T}_{visc}, \qquad (5)$$

where I represents the moment of inertia of the rotating particle, and $\boldsymbol{T}_{visc} = \sum_j \boldsymbol{r}_j \times \boldsymbol{F}_j$ represents the total off-normal torque contribution from the viscous force calculation. For spheres, $I = I_{sphere} = \frac{1}{10} m_p d_p^2$, where m_p is the mass of the particle and d_p is the sphere diameter. Due to floating-point precision errors inherent in performing calculations using quaternions, at the end of each timestep, the quaternion vector is normalized.

C. Particle-particle interaction

Collisions are performed using the inelastic hard-sphere approach, with varying normal coefficients of restitution, e_n. After advection, all particle pairs are checked for a potential collision event. The sole condition for collision is that their intersurfacial distance, H_{kl}, is less than zero. During the timestep which this occurs, the particles collide inelastically and their resulting linear velocities $(\boldsymbol{u}'_{P,1}, \boldsymbol{u}'_{P,2})$ and positions $(\boldsymbol{x}'_{P,1}, \boldsymbol{x}'_{P,2})$ are evaluated as:

$$\boldsymbol{u}'_{P,1} = \boldsymbol{u}_{P,1} \qquad (6)$$
$$+ \frac{m_{P,2}}{m_{P,1} + m_{P,2}} (1 + e) \left(\left(\boldsymbol{u}_{P,2} - \boldsymbol{u}_{P,1} \right) \cdot \hat{\boldsymbol{n}} \right) \hat{\boldsymbol{n}},$$

$$\boldsymbol{u}'_{P,2} = \boldsymbol{u}_{P,2} \qquad (7)$$
$$+ \frac{m_{P,1}}{m_{P,1} + m_{P,2}} (1 + e_n) \left(\left(\boldsymbol{u}_{P,2} - \boldsymbol{u}_{P,1} \right) \cdot \hat{\boldsymbol{n}} \right) \hat{\boldsymbol{n}},$$

$$\boldsymbol{x}'_{P,1} = \boldsymbol{x}_{P,1} + t_{col} \boldsymbol{u}'_{P,1}, \qquad (8)$$

$$\boldsymbol{x}'_{P,2} = \boldsymbol{x}_{P,2} + t_{col} \boldsymbol{u}'_{P,2}. \qquad (9)$$

Intersurface sphere-sphere DLVO forces are calculated to account for van der Waals attraction and electric double layer repulsion (Derjaguin & Landau 1941, Verwey & Overbeek 1955). The equation for the attraction or repulsion caused by a spherical particle, k, on spherical particle, l, is as follows:

$$\boldsymbol{F}_{kl}^{TOTAL} = \boldsymbol{F}_{kl}^{VDV} + \boldsymbol{F}_{kl}^{EDL}. \qquad (10)$$

where F_{kl}^{VDV} is the van der Waals attractive term and F_{kl}^{EDL} is the electric double layer term.

The van der Waals term, which is of great importance in colloidal chemistry, arises due to the electrostatic attraction induced by London dispersion forces (Stenhammar et al. 2010). The electric double layer term arises due to an interfacial pair of ion layers, the first of which screens the second, which are formed on an object when exposed to fluid. The surface charge potential is hence reduced as one moves away from the surface. These two forces are given as:

$$F_{kl}^{VDV} = \frac{-A r_P \hat{n}}{12 H_{kl}^2}, \tag{11}$$

$$F_{kl}^{EDL} = \frac{64 \pi r_P n k_B T_F \Theta^2 e^{-\kappa H_{kl}}}{\kappa} \hat{n}. \tag{12}$$

In the above equations, A is the Hamaker constant, r_P is the particle radius, H_{kl} is the inter-surface distance, n is the number density of electrolyte ions, k_B is Boltzmann's constant, T_F is the fluid temperature, Θ is the reduced surface potential and κ is the inverse Debye length. Note that both of these forces are zero when the intersurfacial distance is less than zero. Finally, $\hat{n}$ is a unit vector pointing from particle k to particle l.

Results and Discussion

A. IBM validation

To establish the validity of the present immersed boundary method, various simulations of immersed stationary spheres at different particle Reynolds numbers were performed to compare calculated drag coefficients with those obtained by empirical investigations.

This validation is similar to that carried out by (Mark & van Wachem, 2008), however it should be noted that in the case of the present work, a much smaller equivalent grid spacing was employed. In the present case, the mesh used to predict isotropic turbulence in the previous subsection was employed, whilst the physical length of the box (relative to the particle) was modified in each case to ensure the cell spacings were sufficient to resolve the flow around the sphere, particularly for increased particle Reynolds numbers.

In each case the sphere diameter was fixed at $d_P = 1.0\ \mu m$ whilst the geometry length varied between 5 and 20 μm. The density of the fluid was 1.0 kgm^{-3} and the kinematic viscosity was 0.1 Nsm^{-2}. The boundary conditions were set such that all boundaries of the box, aside from the outlet, were given a particular velocity, u_∞ (which was varied to obtain different Reynolds numbers). The outlet used a Neumann boundary condition with zero fluid pressure. Simulations were performed using three icosphere subdivision levels in order to determine the effect of this on the accuracy of the predicted drag coefficient. These subdivisions corresponded to $N_F = 20, 80$ and 320, where N_F is the number of triangular faces within the IB mesh.

Fixing the spheres in place, the simulations were allowed to run until the pressure and viscous forces were statistically stationary. These were then used to generate a drag force using the following equation:

$$F_D = F_{viscous} + F_{pressure}. \tag{13}$$

Upon obtaining the drag force, the drag coefficient could be calculated using the equation:

$$C_D = \frac{2}{\rho_F u_\infty^2 \pi r_P^2} |F_D|, \tag{14}$$

which is compared below against the proposed relations based on empirical observations (Stokes 1851, Schiller 1934):

$$C_D = \begin{cases} 24/Re_P & 0 < Re_P \leq 0.5 \\ \dfrac{24}{Re_P}(1 + 0.15 Re_P^{0.687}) & 0.5 < Re_P \leq 1000 \end{cases} \tag{15}$$

with the particle Reynolds number Re_P given by:

$$Re_P = \frac{u_\infty d_p}{\nu_f}. \tag{16}$$

The results of these simulations are presented in Fig. 4. Throughout, the lowest subdivision level particles have their drag coefficients severely underpredicted. This is likely due to the resolution of the mesh and its lack of resemblance to a smooth sphere (which we are comparing against in the equation for drag coefficient). Due to the increase in reference area, these underpredictions are to be expected. As the subdivisions in the mesh are increased, however, we obtain better accuracy when compared to the empirical correlations, particularly at lower particle Reynolds numbers.
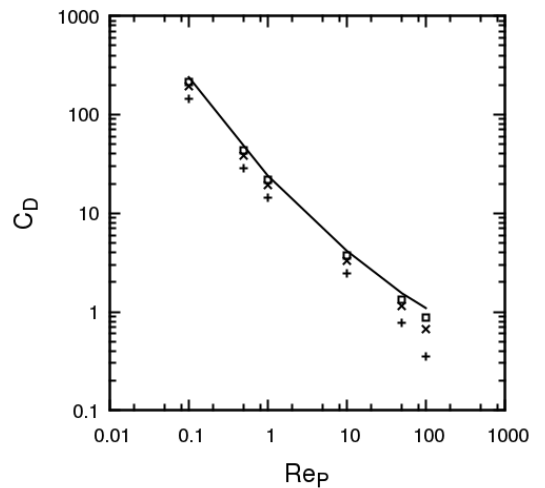

Figure 4: Simulated drag coefficient for icosphere face subdivision $N_F = 20$ (+), $N_F = 80$ (×), and $N_F = 320$ (□) compared against empirical values (solid line).

It is suggested (Mark & van Wachem 2008) that

deviations at higher Reynolds numbers could be due to the particle to domain size ratio, and further studies should be carried out should this method be used to predict the motion of particles at very high Reynolds numbers. In previous channel studies (Rouson & Eaton, 2001), it was observed that particle Reynolds numbers are such that $Re_P < 10$ in all regions of the flow, and so the current validation is sufficient to verify the correct calculation of the drag coefficient for the type of motion of interest in the present work.

B. Behavioural modification

Each simulation was initialized with the particles separated and given a velocity equivalent to a typical pre-collision event in the buffer layer of the channel flow, obtained in previous work (Mortimer et al. 2018). Statistics were gathered over 40 instances of one typical interaction setup, with random injection locations within the isotropic turbulence. These were run for 50 non-dimensional time units. Simulation parameters are presented in Table 2, where e_n is the normal coefficient of restitution, A the Hamaker constant, and Θ the electric double layer reduced surface potential. Simulation 0 represents 'typical' parameters, whilst 1, 2 and 3 are varying e, A and Θ, respectively. The 'typical' parameters were chosen to match calcite particles in water, which is a commonly used simulant in the nuclear industry.

Table 2: Simulation mechanical and chemical properties.

RUN	0	1a	1b	2a	2b	3a	3b
e_n	0.4	0.2	0.6	0.2	0.6	0.4	0.4
$A(zJ)$	22.3	22.3	22.3	7.84	36.76	22.3	22.3
$\Theta(mV)$	20	20	20	20	20	16	24

Figure 5 illustrates a typical event where two particles meet, with the surrounding turbulence field reacting to the presence of the particles and also the collision. Note that the slice is through the particle on the right, indicated by the local velocity matching the velocity of the particle as per the IB condition.
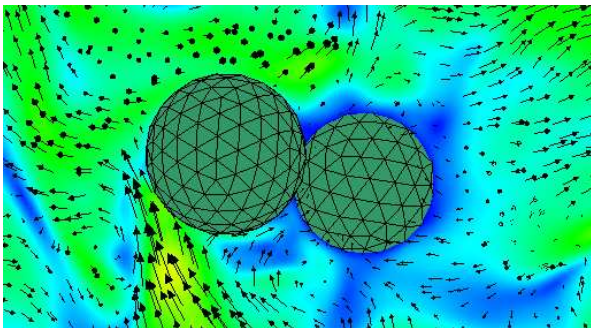

Figure 5: Typical binary particle interaction event with pseudocolour to represent fluid velocity magnitudes plotted alongside fluid velocity vectors.

Figure 6 indicates the sensitivity to the restitution

coefficient by considering the mean relative displacement and mean relative velocity sampled over 40 instances. Separations (dx) are normalized by the particle radius. Clearly this property has a strong effect on collision dynamics. A high e_n means that the particles spend much less time in close proximity to each other, which is a result of their retention of kinetic energy allowing them to overcome the van der Waals attraction, and return back to a region where turbulence dominates. The plot of relative velocity magnitude indicates a larger spread in velocities for increased e_n, which suggests a greater variety of events where particles frequently change their velocity. Certain procedures can modify this parameter such as coating the particles with viscous films (Gollwitzer et al. 2012).
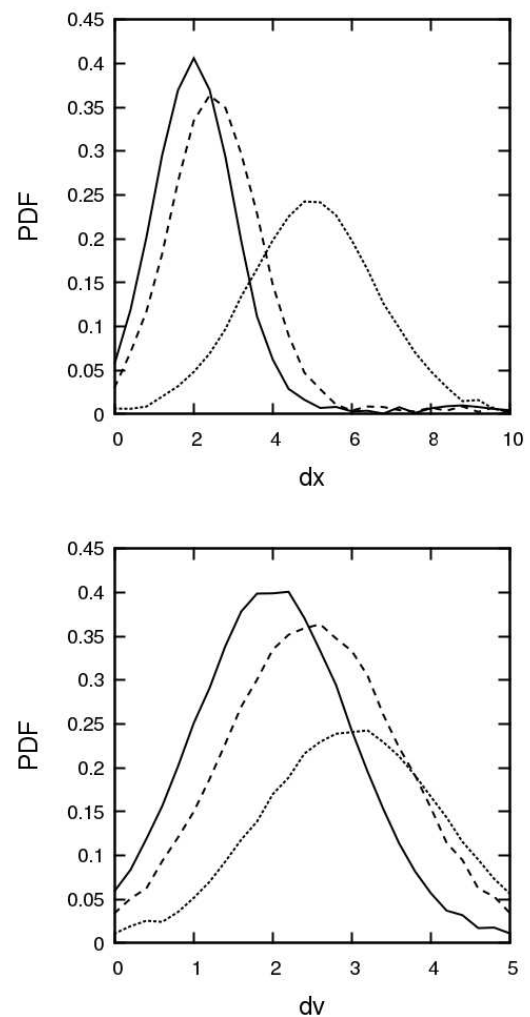

Figure 6: PDFs of relative displacement (upper) and relative velocity (lower) for $e = 0.2$ (solid), $e = 0.4$ (dashed) and $e = 0.6$ (dotted).

The Hamaker constant directly modulates the attraction term in the DLVO potential equation, and as such should, it would be expected, govern the agglomeration rate. In Fig. 7 we observe that actually the Hamaker constant has little effect on the resulting probability density function (PDF) of the relative displacement. This implies that, for the range of values studied, the amount of time particles spend close to

each other is independent of the strength of the attraction. An explanation for this is likely that the particles are undergoing near-hits but then travelling past each other and being carried away by turbulence once they overshoot the attractive region. This would make the agglomeration mechanism less sensitive to the Hamaker constant, since the agglomeration would only depend on the velocity vectors of the particles at the start of the interaction event.

The above explanation is reinforced by the plot of relative velocity. Despite the particles not spending different amounts of time close to each other, they differ quite extensively in velocity, with high Hamaker constants meaning the particles travel faster and at a greater range of speeds. If the particles are shooting past each other then this would be the case since the acceleration and subsequently range of velocities would depend primarily on the attraction strength. This behaviour implies that in high concentration fluid-particle dispersions, the Hamaker constant would also have an effect on decoupling the particles from the local flow velocities, particularly for inertial particles. For low Stokes number particles, or tracers, the forces may cause additional collisions since the attractive forces could cause particle motion to deviate away from the fluid flow streamlines, which could lead to increased agglomeration rates, particularly in the bulk flow region.
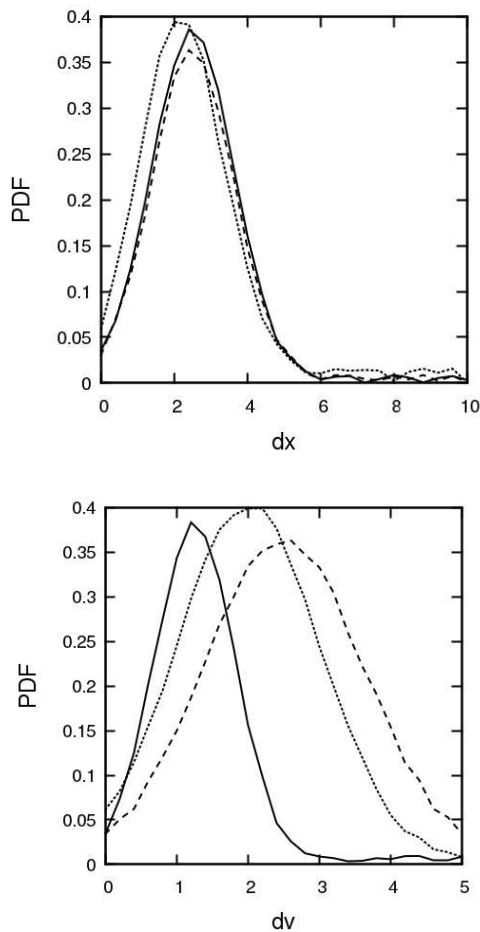

Figure 7: PDFs of relative displacement (upper) and relative velocity (lower) for $A = 17.84$ zJ (solid), $A = 22.3$ zJ (dashed) and $A = 26.76$ zJ (dotted).

In practice, the Hamaker constant has been shown to be adjustable by adding salt to the fluid (Shahidzadeh et al. 1998) and has also been demonstrated to be temperature dependent (Bergström, 1997). By tuning this parameter, one has control over dispersion, collision rate and aggregation of particles in the flow.

Figure 8 illustrates the sensitivity of the relative displacement and relative velocity to the strength of the electric double layer potential. In both plots, it is evident that for the range of parameters considered, there is little effect on the resulting dynamics. This is due to the very short range associated with this force, which is negligible when compared to the length scales associated with both the particles and the turbulence. In order for this force to influence particle-scale motion, the size of the particles would need to be in the nanometre range.
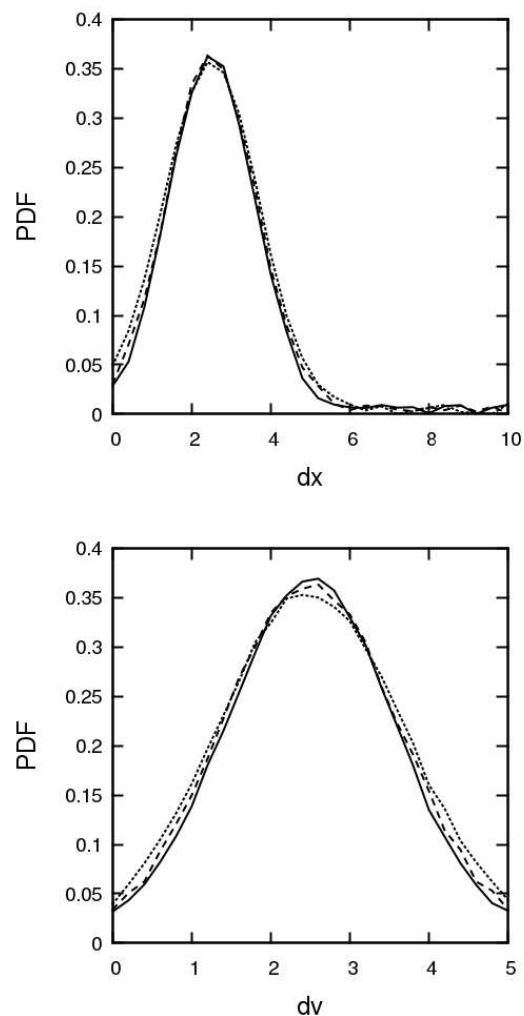

Figure 8: PDFs of relative displacement (upper) and relative velocity (lower) for $\theta = 16$ mV (solid), $\theta = 20$ mV (dashed) and $\theta = 16$ mV (dotted).

Conclusions

A novel second-order accurate IBM has been implemented in the spectral element-based DNS code, Nek5000. The ghost-cell method is used to ensure the no-slip condition on the particle surface is met. A

validation of the IBM has been performed which considers the drag force on a stationary spherical particle subject to flow fields with differing Reynolds numbers. For a high degree of mesh subdivisions on the particle, the calculated drag coefficients agree very well with frequently used empirical correlations.

For the first time, this method has been used to predict binary particle interaction events at fine particle and turbulence scales using DLVO forcing. These techniques have been used to study the effect of varying certain mechanical and chemical parameters on collision and aggregation dynamics.

We observe that increasing the coefficient of restitution leads to reduced aggregation. It is also shown that increasing the Hamaker constant increases the mean speed of the interacting particles, but has little effect on the probability of agglomeration, over the range of values studied. We suggest that in this case the particles are attracted to each other but often do not collide, leading to their reintroduction to regions of turbulence where DLVO forces are low. Finally, varying the electric double layer potential has little effect on the resulting statistics since its magnitude is small compared to other forces, and its effective range is also very short.

The work presented here provides a novel basis for the development of behavioural modification techniques which modify the above parameters of interest in order to obtain, or discourage, certain desired flow properties such as agglomeration, collision and deposition rates.

References

Bergström, L. Hamaker constants of inorganic materials. Adv. Colloid Interface Sci., Vol. 70, pp. 125-169 (1997)

den Toonder, J., Hulsen, M., Kuiken, G. & Nieuwstadt, F. Drag reduction by polymer additives in a turbulent pipe flow: Numerical and laboratory experiments. J. Fluid Mech, Vol. 337, pp. 193-231 (1997)

Derjaguin, B. & Landau, L. Theory of the stability of strongly charged lyophobic sols and of the adhesion of strongly charged particles in solutions of electrolytes. Acta Physicochim, Vol. 14, pp. 633-662 (1941)

Fischer, P.F., Lottes, J.W. & Kerkemeier, S.G. Nek5000 Web page, http://nek5000.mcs.anl.gov (2008)

Gollwitzer, F., Rehber, I., Kruelle, C.A. & Huang, K. Coefficient of restitution for wet particles. Phys. Rev. E., Vol. 86, 011303 (2012)

Gosman, A.D. & Ioannides, E. Aspects of computer simulation of liquid-fueled combustors. J. Energy., Vol. 7, pp. 482-490 (1983)

Hu, H.H., Direct simulation of flows of solid-liquid mixtures. Int. J. Multiphas. Flow, Vol. 22, pp. 335-352 (1996)

Lundgren, T. Linearly forced isotropic turbulence. In Annual Research Briefs (Center for Turbulence Research, Stanford), pp. 461-473 (2003)

Mark, A. & van Wachem, B.G. Derivation and validation of a novel implicit second-order accurate immersed boundary method. J. Comput. Phys., Vol. 227, pp. 6660-6680 (2008)

Mortimer, L.F., Fairweather, M & Njobuenwu, D.O. Near-wall interparticle collision dynamics in multi-phase turbulent channel flows. Proc. 9th Int. Symp. Turbulence, Heat and Mass Transfer, pp. 443-446 (2018)

Peskin, C.S. The immersed boundary method. Acta Numerica, Vol. 11, pp. 479-517 (2002)

Rosales, C. & Meneveau, C. Linear forcing in numerical simulations of isotropic turbulence: Physical space implementations and convergence properties. Phys. Fluids, Vol. 17, 095106 (2005)

Rouson, D.W. & Eaton, J.K. On the preferential concentration of solid particles in turbulent channel flow. J. Fluid Mech.m Vol. 428, pp. 49-169 (2001)

Schiller, L. Neue quantitative Versuche zur Turbulenzentstehung. J. Appl. Math. Mech., Vol. 14, pp. 36-42 (1934)

Shahidzadeh, N., Bonn, D., Ragil, K., Broseta, D. & Meunier, J. Sequence of two wetting transitions induced by tuning the Hamaker constant. Phys. Rev. Lett., Vol. 80, pp.3992-3995 (1998)

Short, M.P., Hussey, D., Kendrick, B., Besmann, T., Stanek, C. & Yip, S. Multiphysics modeling of porous CRUD deposits in nuclear reactors. J. Nucl. Mater., Vol. 443, pp. 579-587 (2013)

Stenhammar, J., Linse, P., Wennerström, H. & Karlström, G. An exact calculation of the van der Waals interaction between two spheres of classical dipolar fluid. J. Phys. Chem. B, Vol. 114, pp. 13372-13380 (2010)

Stokes, G.G. On the effect of the internal friction of fluids on the motion of pendulums. Pitt Press (1851)

Tseng, Y.H. & Ferziger, J.H. A ghost-cell immersed boundary method for flow in complex geometry. J. Comput. Phys., Vol. 192, pp. 593-623 (2003)

Verwey, E.J.W. & Overbeek, J.T.G. Theory of the stability of lyophobic colloids. J. Colloid Sci., Vol. 10, pp. 224-225 (1955)

Walters, D.K. & Luke, W.H. Computational fluid dynamics simulations of particle deposition in large-scale, multigenerational lung models. J. Biomech. Eng., Vol. 133, pp. 011003-011008 (2011)

Wang, J., Shen, Y. & Guo, Y. Seasonal circulation and influence factors of the Bohai Sea: A numerical study based on Lagrangian particle tracking method. Ocean Dynam., Vol. 60, pp. 1581-1596 (2010)